Vacuum birefringence in the polarized X-ray emission of a radio magnetar

- Rachael E. Stewart^{1*†}, Hoa Dinh Thi^{2*†}, George Younes^{3,4*}, Marcus E. Lower^{5*}, Matthew G. Baring^{2*}, Michela Negro⁶, Fernando Camilo⁷, Joel B. Coley⁸, Alice K. Harding⁹, Wynn C. G. Ho¹⁰, Chin-Ping Hu¹¹, Philip Kaaret¹², Paul Scholz¹³, Alex Van Kooten¹, Zorawar Wadiasingh^{14,3}
- ¹Department of Physics, George Washington University, 725 21st Street NW, Washington DC, 20052, District of Columbia, USA.
 - ²Department of Physics and Astronomy, Rice University, 6100 Main Street, Houston, 77251, Texas, USA.
 - ³Astrophysics Science Division, NASA Goddard Space Flight Center, 8800 Greenbelt Road, Greenbelt, 20771, Maryland, USA.
 - ⁴Center for Space Sciences and Technology, University of Maryland Baltimore County, 1000 Hilltop Cir, Baltimore County, 21250, Maryland, USA.
- ⁵Centre for Astrophysics and Supercomputing, Swinburne University of Technology, PO Box 218, Hawthorn, 3122, Victoria, Australia.
- ⁶Department of Physics and Astronomy, Louisiana State University, 202 Nicholson Hall, Baton Rouge, 70803, Louisiana, USA.
- ⁷South African Radio Astronomy Observatory, Liesbeek House, River Park, Cape Town, 7700, South Africa.
- ⁸Department of Physics and Astronomy, Howard University, Washington, DC 20059, USA; CRESST/Mail Code 661, Astroparticle Physics Laboratory, NASA Goddard Space Flight Center, Greenbelt, MD 20771, USA.
- ⁹Theoretical Division, Los Alamos National Laboratory, Los Alamos, 87545, New Mexico, USA.
 - ¹⁰Department of Physics and Astronomy, Haverford College, 370 Lancaster Avenue, Haverford, 19041, Pennsylvania, USA.
- ¹¹Department of Physics, National Changhua University of Education, No. 1, Jinde Rd., Changhua, 500207, Taiwan.
- ¹²NASA Marshall Space Flight Center, Huntsville, 35812, AL, USA.

¹³Department of Physics and Astronomy, York University, 4700 Keele Street, Toronto, MJ3 1P3, ON, Canada.
 ¹⁴Department of Astronomy, University of Maryland, College Park, 20742, MD, USA.

*Corresponding author(s). E-mail(s): raestewart@gwu.edu; hoa.dinh@rice.edu; george.a.younes@nasa.gov; mlower@swin.edu.au; baring@rice.edu;

[†]These authors contributed equally to this work.

Summary paragraph

The quantum electrodynamics (QED) theory predicts that the quantum vacuum becomes birefringent in the presence of ultra-strong magnetic fields [1, 2] - a fundamental effect yet to be directly observed. Magnetars, isolated neutron stars with surface fields exceeding 10¹⁴ G [3], provide unique astrophysical laboratories to probe this elusive prediction [4-6]. Here, we report phase- and energy-resolved X-ray polarization measurements of the radio-emitting magnetar 1E 1547.0-5408 obtained with the Imaging X-ray Polarimetry Explorer (IXPE), in coordination with the Neutron Star Interior Composition Explorer (NICER) and Parkes/Murriyang radio observations. We detect a high phase-averaged polarization degree of 65% at 2 keV, where the surface thermal emission is dominant, rising to nearly 80% at certain rotational phases, and remaining at $\gtrsim 40\%$ throughout the radio beam crossing. We also observe a strong decrease in polarization from 2 keV to 4 keV. Detailed atmospheric radiative transfer modeling, coupled with geometrical constraints from radio polarization, demonstrate that the observed polarization behavior cannot be consistently explained without invoking magnetospheric vacuum birefringence (VB) influences. These observational findings combined with the theoretical results represent compelling evidence for naturally occurring quantum VB. This work marks a significant advance toward confirming this hallmark prediction of QED and lays the foundation for future tests of strong-field quantum physics using next-generation X-ray polarimeters.

Magnetars [3, 7, 8], a class of isolated neutron stars (NS), possess the strongest known magnetic fields in the observable universe ($B_{\rm surface} \sim 10^{14-15}$ G), surpassing the typical field strength of young, rotation-powered pulsars by 1–3 orders of magnitude. The decay of these magnetic fields powers persistent, high-luminosity X-ray emission, which typically peaks between 0.5 keV and 10 keV and reaches $L_X \gtrsim 10^{35}$ erg s⁻¹ (see e.g. [9] for a review). With magnetic field strengths that far exceed the quantum electrodynamic (QED) critical field $B_{\rm cr} = 4.4 \times 10^{13}$ G, magnetars are widely recognized as promising astrophysical laboratories for testing exotic, non-linear QED processes in the strong B-field regime [10, 11].

One such prediction is vacuum birefringence (VB), wherein intense magnetic fields – comparable to those of magnetars – substantially modify the refractive indices of photon polarization eigenmodes and render them disparate: different polarizations propagate at different speeds [12, 13]. This property is a direct consequence of the polarization of the quantum vacuum, and its constituent "virtual" electron-positron pairs, by the electromagnetic field [1, 2], and remains an unverified prediction of QED. Although indirect evidence consistent with the action of VB has been reported both in laboratory contexts [14] and in astrophysical settings [15, 16], direct, unambiguous measurements of VB in either of these settings has remained elusive [11, 15, 17–19]. Together, these complementary approaches offer promising paths to a decisive confirmation of one of the most exotic predictions of QED.

The influence of VB in magnetar magnetospheres is expected to strongly enhance the polarization signature of soft X-ray photons emerging from their surfaces. These photons are predicted to undergo differential phase shifts depending on their two polarization modes – ordinary (O mode) and extraordinary (X mode). If k represents a photon's momentum vector, the O mode (||) has an electric field vector approximately in the k - B plane, and the X mode (\perp) has its electric field perpendicular to this plane. This phenomenon decouples the polarization eigenmodes out to altitudes of $\sim 30-300$ stellar radii, leading to a tight correlation of their polarization vectors with the magnetospheric field morphology. The result is that VB enhances the net linear polarization of surface emission, potentially producing polarization degrees (PDs) approaching 100% under ideal viewing geometries [5, 20, 21]. Inside magnetar atmospheres, the combined influence of vacuum and plasma birefringence allows photons to convert between polarization modes [4, 19]. This mode conversion is most efficient at a QED vacuum resonance energy (typically around a few keV) that depends on the hydrogenic plasma density and the surface field strength, and acts to depolarize the net PD emerging from the surface. Consequently, one expects a rotational-phaseaveraged high PD away from the vacuum resonance energy and strong PD reduction near it due to increased mode mixing.

1E 1547.0–5408 is a canonical magnetar with a spin period of 2.09 s and a surface magnetic field strength of $\approx 2.2 \times 10^{14}$ G [22]. It is currently in a persistently bright X-ray state, exhibiting a typical magnetar spectrum – a soft thermal-like component prominent in the $\lesssim 10$ keV band, and a hard X-ray tail dominating at higher energies [23, 24]. The broadband 0.5–70 keV spectrum is best fit with either a double blackbody (BB) thermal contribution and a non-thermal power-law (PL) model or a single BB and double PL model [23, 24]. The pulse shape at all energies is virtually sinusoidal,

with minimal contribution from higher harmonics. The root-mean-squared (RMS) pulsed fraction [25] is notably large compared to the rest of the magnetar population – it also exhibits a strong energy-dependence with a value of $\sim 30\%$ at 2 keV that steadily increases to 42% around 6 keV, before decreasing monotonically towards 20% at energies > 10 keV [23, 24]. These spectral+timing characteristics likely indicate the presence of a thermal hot spot on the surface dominating the softest energies of the spectrum up to ~ 6 keV, whereafter emission of magnetospheric origin overtakes the spectrum's surface contribution and alters the pulse properties [23, 24].

1E 1547.0-5408 is also unique among the magnetar population as a persistent radio pulsar [26]. It emits broad radio pulses at the spin-period of the magnetar, spanning approximately 25% of the source duty cycle (Methods), unusually wide among the young, isolated NS population. The pulses are also highly polarized and display a characteristic S-shaped swing in the linear polarization position angle (PA) [26], indicative of the viewing line-of-sight crossing the radio emission cone. These properties hint at a nearly-aligned rotator, with an observer line-of-sight at a small angle to the rotation axis that samples open magnetic field lines proximate to the polar cap (Methods).

This richness of information offered by the combined X-ray + radio data motivated a deep simultaneous observing campaign with the Imaging X-ray Polarimetry Explorer (IXPE), the Neutron star Interior Composition ExploreR (NICER), and *Murriyang*, the 64 m Parkes radio telescope, which was carried out between March 26, 2025 UTC 03:01:52 and April 5, 2025 UTC 00:26:53. Our ultimate goal is to study in detail the soft (2–8 keV) X-ray polarimetric properties of the source as afforded by IXPE and to place it in context of the geometrical constraints achievable through the radio observations. Hence, all of the observations were coordinated to optimize simultaneous coverage between the instruments, particularly with IXPE (see Methods for full details of the observations).

The IXPE data reveal an energy and phase-averaged 2–8 keV PD of about $46\pm4\%$ (1 σ uncertainty; here and throughout the rest of the text) with a polarization angle (PA) of $-76^{\circ}\pm3^{\circ}$ (Figure 1) with a statistical significance of $\sim 10.5\sigma$ above the minimum detectable polarization value for the 99% confidence level (MDP₉₉). This is the largest such PD in the population of six IXPE-observed magnetars [11, 27, 28]. The PD also displays strong energy dependence, achieving a maximum at $59\pm5\%$ in the softest energy band of 2–3 keV before decreasing to $37\pm5\%$ in the 3–4 keV range. The PA of the two bands, on the other hand, remain consistent with that of the energy-integrated measurement. In the hard part of the energy range (4–8 keV), we measure a PD of $40\pm11\%$, and slightly shifted PA of $-86^{\circ}\pm8^{\circ}$, a detection at only the 3.5σ significance level, mainly due to its lower signal-to-noise. Notably, the PD of the softest energy range is at least a factor of 2.5 larger than the corresponding values measured in the rest of the population [28].

Using a phase-coherent timing ephemeris that covers our full observing campaign, we phase-fold the X-ray (intensity and polarization) and radio data, after correcting for propagation through the ionized interstellar medium to ensure absolute alignment between the two wavelengths (see Methods). The PD is most prominent in the softer part of the spectrum (Figure 2). It modulates moderately with phase, reaching a peak

of $74\pm11\%$ in the 2–4 keV range and a minimum of about $34\pm8\%$; the former occurs close to the X-ray pulse minimum and away from the radio pulse, in contrast to the latter. Note that the PD reaches $82\pm15\%$ in the 2–3 keV range and a minimum of $42\pm12\%$: see Extended Figure 7. The PA displays a sinusoidal modulation between a maximum of $-51^{\circ}\pm6^{\circ}$ and a minimum of $-97^{\circ}\pm9^{\circ}$. The latter occurs around the minimum radio PA which also reaches similar values.

Finally, the spectro-polarimetric analysis of the IXPE+NICER phase-averaged spectrum reveals that the emission in the soft 1–8 keV X-ray band is best described by a BB component with a temperature $kT = 0.72 \pm 0.01$ keV and a relatively small emitting area $R^2 = 1.07 \pm 0.05$ km² (see Methods), assuming a source distance of 4.5 kpc [29]. In accentuating the model-independent polarization results presented above, we find that the phase-averaged BB polarization Q and U spectra are best modeled by a linearly decreasing PD from $65 \pm 8\%$ at 2 keV at a rate of $-15 \pm 2\%$ keV⁻¹, and a constant PA of $-67^{\circ}_{-7}^{+4}$. We do not find evidence of changing PA or PD trend at the upper-end of the IXPE energy band ($\gtrsim 5$ keV), as hinted at (albeit at a low significance) in our model-independent analysis. This is likely due to the fact that the 2–8 keV IXPE source spectrum is heavily dominated by the 2–5 keV range where the source is most prominently detected; indeed, adding a second component to the spectrum is not statistically justified, and, when included, remains unconstrained (see Methods).

The modest phase-averaged PD measured for most magnetars in the soft, 2–3 keV X-ray band $[\lesssim 20\%, 28]$ have so far been interpreted as a sign for the presence of a condensed surface [16, 30]. The much higher PD we measure nominally argues against such a scenario in 1E 1547.0-5408. Indeed, given the high surface temperature reported here and elsewhere [23, 24] and typical dipole magnetic field strength, a magnetic condensation is unlikely for 1E 1547.0-5408 [31]. Phase-averaged polarization degrees approaching 40% may be attainable in a pure magnetized atmosphere without any QED corrections, but obtaining PDs of $\approx 65\%$ would be nontrivial [6]. More problematic for a magnetized atmosphere are the extreme phase-resolved PDs ($\approx 70-80\%$ in the 2-4 keV band: see Figure 2) and the absence of strong depolarization near the radio pulse phase. Nominally, considerable net X-ray depolarization should arise when sampling polar open field lines [32] during the radio beam crossing (discussed below). Yet, while we indeed detect a minimum X-ray PD during the radio pulse, it is still highly polarized at $\approx 30\text{-}40\%$. The action of VB in 1E 1547.0-5408 naturally addresses these inconsistencies: it both enhances the intrinsic PD and suppresses mode mixing, limiting X-ray depolarization along open field lines and preserving polarization signatures beyond the light cylinder [19].

The linear decrease in PD within the narrow energy range of 2–4 keV is notable. A separate, and differently polarized component contributing to the BB emission is ruled out by the spectral and timing properties of the source which argue for the same thermal component dominating these energies. This behavior is most naturally attributed to mode conversion close to vacuum resonance [4, 19]. Given the B-field strength of 1E 1547.0–5408, and assuming a hydrogen atmosphere, mode conversion becomes efficient at energies $\gtrsim 1.5 \text{ keV}$ [31], while the vacuum and plasma contributions to the dielectric tensor become comparable in magnitude and opposite in sign

around 6 keV, consistent with the energy at which the PD value of the BB is expected to reach 0 according to the spectro-polarimetric results.

We test our qualitative picture presented above with detailed modeling of the radio and X-ray pulse and polarization properties. The observed S-shaped sweep of the radio PA across the time and frequency averaged 2.5–4.0 GHz profile in Figure 2 (top) is consistent with the rotating vector model (RVM) for a pure dipolar field geometry [33]. We recover a magnetic and spin axes that are offset by only $\alpha = 2.4^{\circ}_{-1.2}^{+1.4}$, along with the angle between the spin axis and our line of sight of $\zeta = 5.2^{\circ}_{-2.6}^{+3.2}$; this constitutes an aligned rotator viewed close to the spin axis. Under the simplifying assumption that the open field lines above the polar cap are fully illuminated, this combination of the magnetic and viewing geometry along with the high pulse duty cycle suggest the radio emission originates around 330^{+521}_{-245} km above the NS surface (Methods). This height is less than 1% of the light cylinder, and thus the absolute radio pulse phase accurately describes a magnetic pole crossing. We can combine these constraints on the geometry with detailed modeling of the X-ray intensity, Stokes Q/I, and U/I profiles using the atmospheric radiative transfer Monte Carlo simulation, MAGTHOMSCATT [32, 34], to interpret the IXPE measurements.

For the modeling of X-ray pulsations, we considered various single hot spot scenarios; see Methods for details and χ^2 values. General relativistic [35] and VB influences (polarization mode decoupling at low to moderate altitudes) on the magnetospheric propagation of light from the stellar surface to a distant observer are treated in our present, upgraded MAGTHOMSCATT simulation. This code does not yet include mode conversion at the vacuum resonance [4] that arises at higher densities with hotter gas deeper in the stratified atmosphere. Thus, we limited our comparisons to the 2-3 keV data, sampling photons that mostly originate from the cooler outer atmospheric layers where the vacuum resonance effect is expected to be less influential. Among all the cases considered, the best fit $(\chi^2_{\rm tot} \approx 122 \text{ for } 89 \text{ d.o.f.})$ to the intensity, Stokes Q/I and U/I data correspond to a wedged-shaped hot spot spanning from the magnetic pole to 17° in colatitude and covering 120° in longitude abutting the meridional plane on one side (see the blue region in Figure 8), and the optimal geometry was provided by an $\alpha = 0^{\circ}$ and $\zeta = 1.5^{\circ}$. This best fit includes magnetospheric VB influences: see Figure 3 and the blue curves therein. These parameters approximately support the aligned rotator geometry revealed by the radio intensity and the RVM.

Alternatively, a circular offset hot spot of radius $\theta_{\rm cap} = 10^{\circ}$ (see the green region in Figure 8) with its center located at colatitude $\theta_{\rm c} = 17.5^{\circ}$ and longitude $\phi_{\rm c} = 180^{\circ}$ (see Extended Figure 9, bottom row) with $(\alpha, \zeta) = (2^{\circ}, 5.5^{\circ})$ produces an acceptable fit to the intensity while matching our constraints on the magnetic and viewing geometry from the radio polarization. However, the pulsation traces of both Q/I and U/I in this case do not match the data well.

As shown by Figure 3, in the absence of VB (orange solid curves) the Q/I and U/I traces show strong oscillations, a consequence of the convolution of magnetic field directions on the stellar surface. The overall fit quality improves with the inclusion of VB (blue solid curves) for both the wedge and the circular hot spot scenarios (see also Figure 9). In addition, we verified that the observed X-ray PA can be fit with a RVM, and the best-fit geometric parameters are consistent with those obtained

from the radio analysis. This indicates that the X-ray PA data can be described as a purely geometrical effect, a signature of mode-locking due to VB at altitudes up to the polarization limiting radius.

It is notable that for both the optimal wedge solution and the offset circular zone model, the centroids for the X-ray hot spots are at longitudes (60° for the wedge) substantially removed from the meridional plane containing the rotation and magnetic axes (zero longitude), which serves as the central plane of symmetry for the radio RVM model. This naturally delivers a phase lag of the X-ray pulse peak relative to the radio pulse that is broadly consistent with that evinced in Figure 2. The dipolar field lines defining the magnetic flux tube that anchors the radio beam nominally thread the surface only near the periphery of the X-ray hot spots. For the surface footpoints of this radio flux tube to be approximately coincident with the X-ray centroids would require a strong non-poloidal field line shear that would be broadly commensurate with the popular paradigm of field twists in magnetars [36, 37].

The combined insights from these unique X-ray and radio observational results and the theoretical modeling present the most compelling indication of naturally-occurring VB in an astrophysical setting to date. These include phase-averaged polarization degrees reaching $65 \pm \%8$ at 2 keV, rising to $82 \pm 15\%$ at certain rotational phases, and the absence of significant depolarization during the radio pulse. The observed steep decrease in polarization between 2–4 keV is also qualitatively consistent with the expected influence of vacuum resonance. If the actual phase-averaged polarization degree in 1E 1547.0–5408 exceeds 80% between 0.5–1 keV, as suggested by our spectropolarimetric modeling, the presence of VB affecting magnetar surface emissions would be observationally definitive. Future X-ray polarimetric missions such as GoSOX [38] will be essential for accessing this very soft X-ray domain. Together with laboratory and collider-based efforts, and more extensive observations by IXPE, such initiatives will complete the multi-pronged experimental campaign to directly verify one of the most fundamental predictions of quantum electrodynamics.

References

- [1] Heisenberg, W. & Euler, H. Folgerungen aus der Diracschen Theorie des Positrons. Zeitschrift fur Physik 98, 714–732 (1936).
- [2] Schwinger, J. On Gauge Invariance and Vacuum Polarization. *Physical Review* 82, 664–679 (1951).
- [3] Kouveliotou, C. et al. An X-ray pulsar with a superstrong magnetic field in the soft γ -ray repeater SGR1806 20. Nature **393**, 235–237 (1998).
- [4] Lai, D. & Ho, W. C. Polarized X-Ray Emission from Magnetized Neutron Stars: Signature of Strong-Field Vacuum Polarization. *Physical Review Letters* 91, 071101 (2003).
- [5] van Adelsberg, M. & Perna, R. Soft X-ray polarization in thermal magnetar emission. MNRAS 399, 1523–1533 (2009).

- [6] Taverna, R., Turolla, R., Suleimanov, V., Potekhin, A. Y. & Zane, S. X-ray spectra and polarization from magnetar candidates. MNRAS 492, 5057–5074 (2020).
- [7] Duncan, R. C. & Thompson, C. Formation of very strongly magnetized neutron stars Implications for gamma-ray bursts. *ApJL* **392**, L9–L13 (1992).
- [8] Paczynski, B. GB 790305 as a very strongly magnetized neutron star. actaa 42, 145–153 (1992).
- [9] Kaspi, V. M. & Beloborodov, A. M. Magnetars. Annual Review of Astronomy and Astrophysics 55, 261–301 (2017).
- [10] Harding, A. K. & Lai, D. Physics of strongly magnetized neutron stars. *Reports on Progress in Physics* **69**, 2631–2708 (2006).
- [11] Taverna, R. & Turolla, R. X-ray Polarization from Magnetar Sources. *Galaxies* 12, 6 (2024).
- [12] Adler, S. L. Photon splitting and photon dispersion in a strong magnetic field. Annals of Physics 67, 599–647 (1971).
- [13] Tsai, W.-Y. & Erber, T. Propagation of photons in homogeneous magnetic fields: Index of refraction. *Physical Review D* **12**, 1132–1137 (1975).
- [14] Adam, J. et al. Measurement of e⁺e⁻ Momentum and Angular Distributions from Linearly Polarized Photon Collisions. *Physical Review Letters* **127**, 052302 (2021).
- [15] Ho, W. C. G., Lai, D., Potekhin, A. Y. & Chabrier, G. Atmospheres and Spectra of Strongly Magnetized Neutron Stars. III. Partially Ionized Hydrogen Models. Ap.J 599, 1293–1301 (2003).
- [16] Taverna, R. et al. Polarized x-rays from a magnetar. Science 378, 646–650 (2022).
- [17] Ho, W. C. G. & Lai, D. Atmospheres and spectra of strongly magnetized neutron stars II. The effect of vacuum polarization. *MNRAS* **338**, 233–252 (2003).
- [18] Ejlli, A. et al. The PVLAS experiment: A 25 year effort to measure vacuum magnetic birefringence. Physics Reports 871, 1–74 (2020).
- [19] Lai, D. IXPE detection of polarized X-rays from magnetars and photon mode conversion at QED vacuum resonance. Proceedings of the National Academy of Science 120, e2216534120 (2023).
- [20] Heyl, J. S. & Shaviv, N. J. Polarization evolution in strong magnetic fields. MNRAS 311, 555–564 (2000).

- [21] Heyl, J. S., Shaviv, N. J. & Lloyd, D. The high-energy polarization-limiting radius of neutron star magnetospheres I. Slowly rotating neutron stars. *MNRAS* **342**, 134–144 (2003).
- [22] Camilo, F., Ransom, S. M., Halpern, J. P. & Reynolds, J. 1E 1547.0-5408: A Radio-emitting Magnetar with a Rotation Period of 2 Seconds. ApJL 666, L93– L96 (2007).
- [23] Coti Zelati, F. et al. The long-term enhanced brightness of the magnetar 1E 1547.0-5408. A&A **633**, A31 (2020).
- [24] Lower, M. E. et al. The 2022 High-energy Outburst and Radio Disappearing Act of the Magnetar 1E 1547.0-5408. Ap.J 945, 153 (2023).
- [25] Bildsten, L. et al. Observations of Accreting Pulsars. ApJs 113, 367–408 (1997).
- [26] Camilo, F., Reynolds, J., Johnston, S., Halpern, J. P. & Ransom, S. M. The Magnetar 1E 1547.0-5408: Radio Spectrum, Polarimetry, and Timing. Ap.J 679, 681–686 (2008).
- [27] Stewart, R. et al. X-Ray Polarization of the Magnetar 1E 1841-045. ApJL 985, L35 (2025).
- [28] Rigoselli, M. *et al.* IXPE Detection of Highly Polarized X-Rays from the Magnetar 1E 1841-045. *ApJL* **985**, L34 (2025).
- [29] Tiengo, A. et al. The Dust-scattering X-ray Rings of the Anomalous X-ray Pulsar 1E 1547.0-5408. ApJ 710, 227–235 (2010).
- [30] Heyl, J. *et al.* The detection of polarized X-ray emission from the magnetar 1E 2259+586. *MNRAS* **527**, 12219–12231 (2024).
- [31] Medin, Z. & Lai, D. Condensed surfaces of magnetic neutron stars, thermal surface emission, and particle acceleration above pulsar polar caps. *MNRAS* **382**, 1833–1852 (2007).
- [32] Dinh Thi, H., Baring, M. G., Hu, K., Harding, A. K. & Barchas, J. A. Monte Carlo Simulations of Polarized Radiative Transfer in Neutron Star Atmospheres. ApJ in press arXiv:2508.00225 (2025).
- [33] Radhakrishnan, V. & Cooke, D. J. Magnetic Poles and the Polarization Structure of Pulsar Radiation. *Astrophysical Letters* **3**, 225 (1969).
- [34] Barchas, J. A., Hu, K. & Baring, M. G. Polarized Radiation Transfer in Neutron Star Surface Layers. *MNRAS* **500**, 5369–5392 (2021).
- [35] Hu, K., Baring, M. G., Barchas, J. A. & Younes, G. Intensity and Polarization Characteristics of Extended Neutron Star Surface Regions. *ApJ* **928**, 82 (2022).

- [36] Thompson, C., Lyutikov, M. & Kulkarni, S. R. Electrodynamics of Magnetars: Implications for the Persistent X-Ray Emission and Spin-down of the Soft Gamma Repeaters and Anomalous X-Ray Pulsars. *ApJ* **574**, 332–355 (2002).
- [37] Chen, A. Y. & Beloborodov, A. M. Particle-in-Cell Simulations of the Twisted Magnetospheres of Magnetars. I. ApJ 844, 133 (2017).
- [38] Marshall, H. L. et al. O'Dell, S. L., Gaskin, J. A. & Pareschi, G. (eds) The Globe Orbiting Soft X-ray (GOSoX) polarimeter concept study. (eds O'Dell, S. L., Gaskin, J. A. & Pareschi, G.) Optics for EUV, X-Ray, and Gamma-Ray Astronomy X, Vol. 11822 of Society of Photo-Optical Instrumentation Engineers (SPIE) Conference Series, 1182200 (2021).
- [39] Weisskopf, M. C. et al. The Imaging X-Ray Polarimetry Explorer (IXPE): Pre-Launch. Journal of Astronomical Telescopes, Instruments, and Systems 8, 026002 (2022).
- [40] Di Marco, A. et al. Handling the Background in IXPE Polarimetric Data. AJ **165**, 143 (2023).
- [41] Luo, J. et al. PINT: High-precision pulsar timing analysis package (2019). ascl:1902.007.
- [42] Baldini, L. et al. ixpeobssim: A simulation and analysis framework for the imaging X-ray polarimetry explorer. SoftwareX 19, 101194 (2022).
- [43] Hobbs, G. et al. An ultra-wide bandwidth (704 to 4 032 MHz) receiver for the Parkes radio telescope. PASA 37, e012 (2020).
- [44] Hotan, A. W., van Straten, W. & Manchester, R. N. PSRCHIVE and PSRFITS: An Open Approach to Radio Pulsar Data Storage and Analysis. PASA 21, 302–309 (2004).
- [45] van Straten, W., Demorest, P. & Oslowski, S. Pulsar Data Analysis with PSRCHIVE. Astronomical Research and Technology 9, 237–256 (2012).
- [46] Lower, M. E., Shannon, R. M., Johnston, S. & Bailes, M. Spectropolarimetric Properties of Swift J1818.0-1607: A 1.4 s Radio Magnetar. ApJL 896, L37 (2020).
- [47] Hobbs, G. B., Edwards, R. T. & Manchester, R. N. TEMPO2, a new pulsar-timing package I. An overview. MNRAS 369, 655–672 (2006).
- [48] Edwards, R. T., Hobbs, G. B. & Manchester, R. N. TEMPO2, a new pulsar timing package - II. The timing model and precision estimates. MNRAS 372, 1549–1574 (2006).
- [49] Everett, J. E. & Weisberg, J. M. Emission Beam Geometry of Selected Pulsars Derived from Average Pulse Polarization Data. Ap.J 553, 341–357 (2001).

- [50] Wilms, J., Allen, A. & McCray, R. On the Absorption of X-Rays in the Interstellar Medium. ApJ 542, 914–924 (2000).
- [51] Verner, D. A., Ferland, G. J., Korista, K. T. & Yakovlev, D. G. Atomic Data for Astrophysics. II. New Analytic FITS for Photoionization Cross Sections of Atoms and Ions. ApJ 465, 487 (1996).
- [52] Ashton, G. et al. BILBY: A User-friendly Bayesian Inference Library for Gravitational-wave Astronomy. ApJs 241, 27 (2019).
- [53] Speagle, J. S. DYNESTY: a dynamic nested sampling package for estimating Bayesian posteriors and evidences. *MNRAS* **493**, 3132–3158 (2020).
- [54] Gil, J., Gronkowski, P. & Rudnicki, W. Geometry of the emission region of PSR 0950+08. A&A 132, 312-316 (1984).
- [55] Rankin, J. M. Toward an Empirical Theory of Pulsar Emission. IV. Geometry of the Core Emission Region. *ApJ* **352**, 247 (1990).
- [56] Johnston, S. et al. The Thousand-Pulsar-Array programme on MeerKAT XI. Application of the rotating vector model. MNRAS 520, 4801–4814 (2023).
- [57] Lower, M. E., Johnston, S., Shannon, R. M., Bailes, M. & Camilo, F. The dynamic magnetosphere of Swift J1818.0-1607. MNRAS 502, 127–139 (2021).
- [58] Desvignes, G. et al. A freely precessing magnetar following an X-ray outburst. Nature Astronomy 8, 617–627 (2024).
- [59] van Adelsberg, M. & Lai, D. Atmosphere models of magnetized neutron stars: QED effects, radiation spectra and polarization signals. *MNRAS* **373**, 1495–1522 (2006).
- [60] Lai, D. & Ho, W. C. G. Resonant Conversion of Photon Modes Due to Vacuum Polarization in a Magnetized Plasma: Implications for X-Ray Emission from Magnetars. Ap.J 566, 373–377 (2002).
- [61] Deller, A. T., Camilo, F., Reynolds, J. E. & Halpern, J. P. The Proper Motion of PSR J1550-5418 Measured with VLBI: A Second Magnetar Velocity Measurement. ApJL 748, L1 (2012).

1 Figures

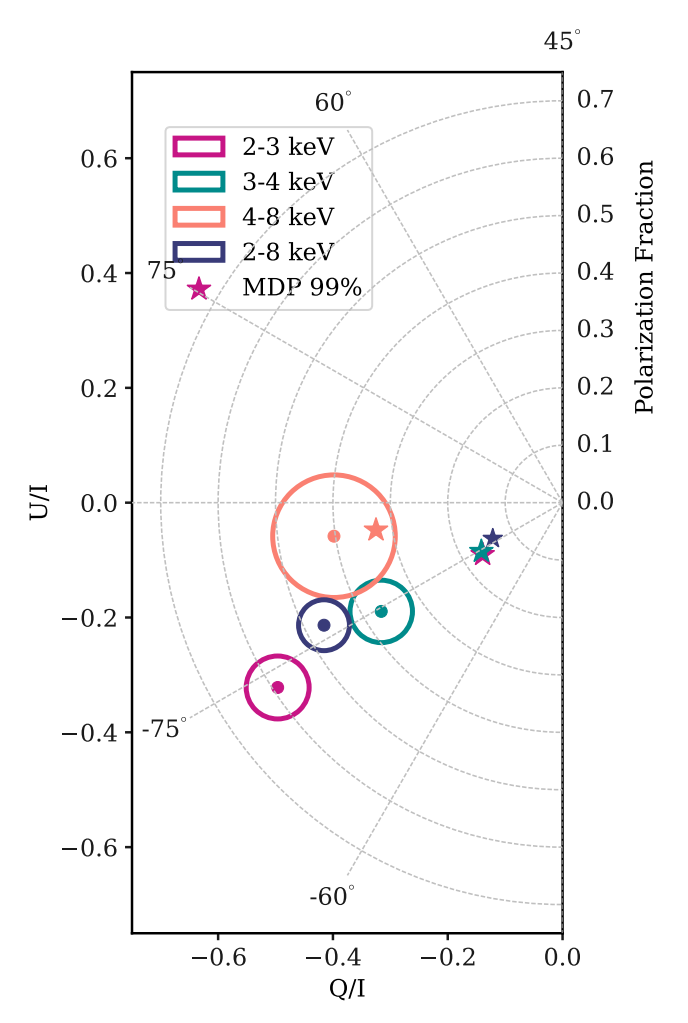


Fig. 1 Background-subtracted and phase-averaged polarization measurements of 1E 1547.0–5408. We display the PD in 4 energy bands, 2–3, 3–4, 4–8, and 2–8 keV. Contours show the 68.3% (1σ) confidence regions for Stokes Q/I and U/I (polarization degree and angle are shown in the radial and polar lines, respectively). The stars display the corresponding minimum detectable polarization at the 99% confidence level (MDP99) for each energy bin. The 2–8 keV energy-integrated polarization characteristics are shown in dark blue. Notably, the energy-integrated PD (dark blue) is 46% and the 2–3 keV PD (magenta) reaches 59%. The PD decreases substantially in the energy range 3–4 keV. The PD remains high at 40% in the 4–8 keV band, yet it suffers from a considerably lower signal-tonoise ratio (S/N). The PA does not exhibit strong variation across energy.

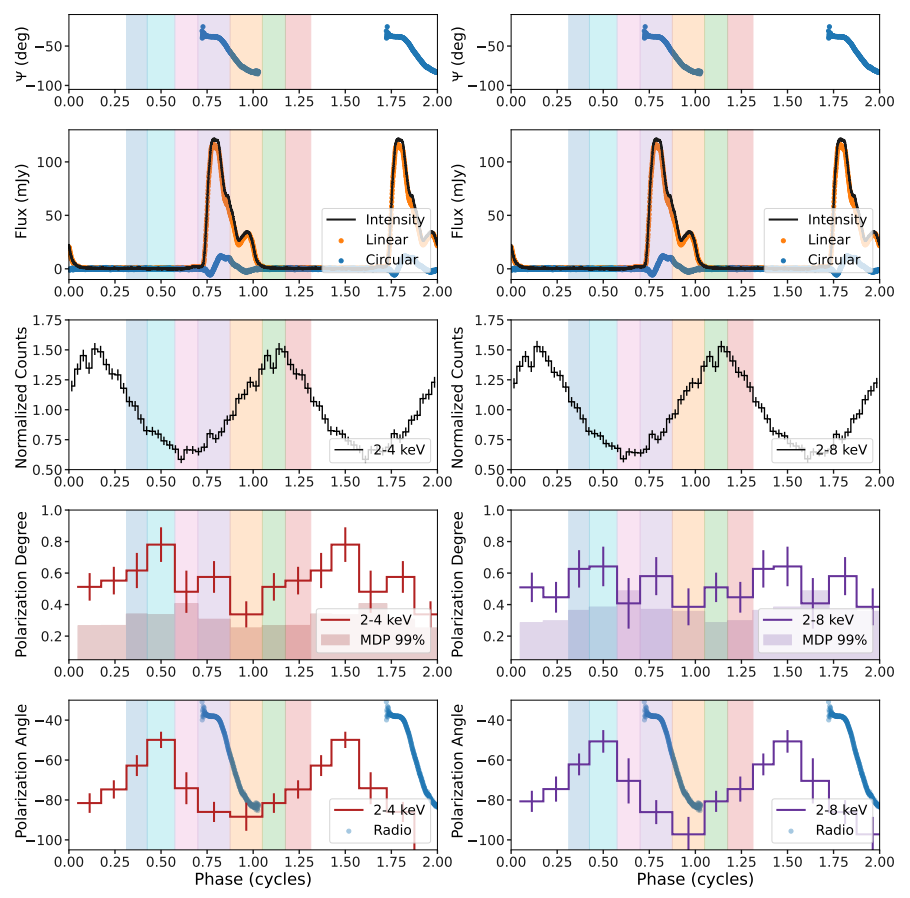


Fig. 2 Phase-resolved radio and X-ray polarization characteristics of 1E 1547.0—5408. The uppermost row shows the radio polarization angle (two cycles shown for clarity). The second row displays the radio intensity curve (black) along with the total linear radio polarization (orange) as well as the circular radio polarization (blue). All of the shown radio data are averaged across our three Murriyang observations. The bottom three rows show the IXPE intensity, polarization degree, and polarization angle pulse profiles, respectively. The radio PA is also displayed in the bottom panel for ease of comparison to the X-ray PA. The IXPE pulse profiles are displayed according to two energy bands: 2–4 keV (left column) and 2–8 keV (right column). The shaded curves overlaying the polarization degree panels depict the MDP₉₉ at each corresponding phase bin. The vertical colored bands highlight the binning used for the IXPE phase-resolved polarization analysis.

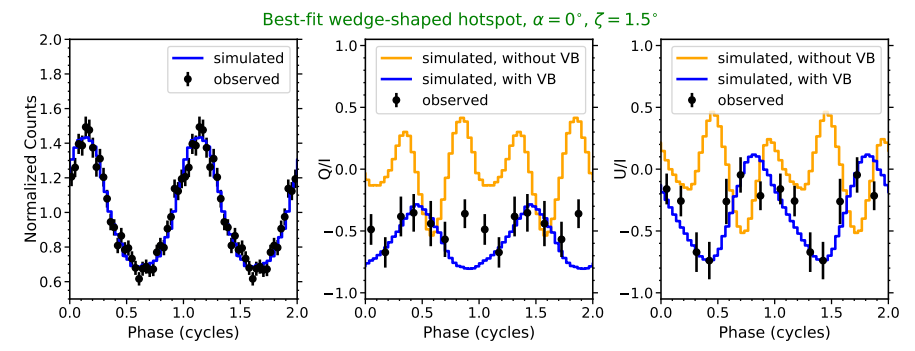


Fig. 3 Simulated intensity (left) and Stokes Q/I (center) and U/I (right) pulse profiles from MAGTHOMSCATT for a single hot spot wedge offset from the magnetic pole as a function of rotational phase (solid lines). The black dots represent the intensity (left), Stokes Q/I (center), and U/I (right) data extracted from IXPE in the 2–3 keV energy range. The case with the best statistical fit (lowest combined total χ^2 ; see Methods) incorporates vacuum birefringence, and corresponds to a magnetic colatitude of $\theta_m = [0^\circ, 17^\circ]$ and longitude $\phi_m = [0^\circ, 120^\circ]$ (zero longitude contains the rotation and magnetic axes); it is displayed in blue. The orange solid curves on the center and right panel show the corresponding polarization profiles wherein VB is turned off – these fits are statistically worse than those with VB on (see Methods).

2 Tables

Table 1 Spectro-polarimetric model

Value $\pm~1\sigma$
$3.67 \times 10^{22} \text{ (fixed)}$
0.80 ± 0.08
0.15 ± 0.02
-67^{+4}_{-7}
-4 ± 4
0.720 ± 0.005
1.07 ± 0.05
1.0 (fixed)
1.08 ± 0.05
1.05 ± 0.05
1.01 ± 0.05
0.80 ± 0.03
0.80 ± 0.03
0.76 ± 0.03
1798.80 with 1511 d.o.f.

Spectral and polarimetric parameters for the best fit model, a single absorbed blackbody (BB) with linearly varying polarization. A multiplicative cross-calibration uncertainty is also added to the model. All uncertainties are calculated at the 68.3% confidence level (1σ) . The fit statistic employs a combination of the C-stat and Chi-Squared statistics used for NICER and IXPE, respectively. Blackbody emitting radius is derived adopting a distance of 4.5 kpc [29].

3 Methods

3.1 IXPE data reduction

The Imaging X-ray Polarimetry Explorer (IXPE), launched in December 2021, is the first imaging X-ray polarimetry space observatory. IXPE consists of three identical telescopes sensitive to 2–8 keV with detector units (DU) containing a Gas Pixel Detector (GPD) that images the photoelectron tracks from incoming X-rays [39]. IXPE observed the magnetar 1E 1547.0-5408 between UTC 2025-03-26T03:01:52 (MJD 60760.12629630) and UTC 2025-04-05T00:26:53 (MJD 60770.01866898) for a total livetime duration of 499.5 ks (see Table 3). We applied background rejection via the treatment recommended in [40] using the software filter_background.py. No significant solar flaring or bursting activity was detected during this observation. The total number of counts detected in the full IXPE band is 20943. We performed the solar-system barycenter correction of the data using the HEASoft version 6.35 task barycorr according to source coordinates (237.725517, -54.306697) with the JPL planetary ephemeris DE405. We subsequently used the pulsar timing package, PINT [41], to assign phases to each photon according to a phase-coherent timing solution that incorporated both radio and X-ray time of arrivals (ToAs) (see Extended Table 4 for details of the full timing solution).

After using DS9 to identify the peak of the centroid of the IXPE observation as being (474.37962, 563.01254), we utilized the software ixpeobssim version 31.0.1 to perform data cleaning and extract high level data products, including spectra, lightcurves, and binned polarization cubes. The ixpeobssim task xpradialprofiles allowed us to examine the radial profiles and identify the extraction region size that optimized the data's signal-to-noise ratio. Based on the radial profiles, we selected a circular source region of 0.5' and an annular background with an inner radius of 2.5' and outer radius of 4.5'. For the energy and phase-resolved products, we select the instrument response functions (IRFs) as ixpe:obssim*:v13 from ixpeobssim's pseudo-CALDB which provides the arf, rmf, PSF, vignetting functions, modulation factors, and modulation responses corresponding to the observation date [42]. For the spectral products, we generated the arf, rmf, and mrf for each detector via the HEASoft tool ixpecalcarf and uploaded each corresponding response to Xspec during the spectral fitting.

The intensity X-ray pulse profiles are binned according to 32 equally spaced bins. The phase-resolved polarization degree and angle, on the other hand, were calculated according to 7 inhomogeneous phase bins to sample the morphology seen in both the radio and the X-ray intensity profiles.

3.2 NICER data reduction

The Neutron star Interior Composition Explorer (NICER) is a non-imaging soft X-ray telescope aboard the International Space Station sensitive between $0.2-12~\rm keV$ with an effective collecting area of $1900~\rm cm^2$ peaking at $1.5~\rm keV$. Its superior timing resolution of < 300 nanoseconds makes NICER ideal for tracking magnetar temporal behavior. The data was extracted and cleaned using the HEASoft version 6.35

tool NICERDAS version 13a; the files were calibrated with NICER CALDB version 20240206. We applied standard filtering via the nicer12 task. Each photon time of arrival was barycenter corrected to the solar system according to the JPL solar-system ephemeris DE405 using the HEASoft tool barycorr. We generated the lightcurves and spectra using the task nicer13, including the NICER spectral background model, SCORPEON which can be simultaneously fit with the source spectra to model sky and non-X-ray background contributions.

3.3 Parkes/Murriyang data reduction

We conducted three observations of 1E 1547.0-5408 concurrent to the IXPE campaign using Murriyang, the 64 m Parkes radio telescope, with the Ultra-Wideband Low (UWL) receiver system [43]. These observations were collected as part of the longterm Parkes Magnetar Monitoring Programme (project ID: P885). We recorded full Stokes pulsar fold-mode data using the MEDUSA signal processor, where the voltage stream was coherently de-dispersed at $697\,\mathrm{pc\,cm^{-3}}$ to correct for signal dispersion in the interstellar medium and then folded at the rotation period of the magnetar with 1024 phase bins covering each rotation of the magnetar. The data were subsequently averaged in time to form 30 s duration sub-integrations, each containing 3328 frequency channels covering the 704-4032 MHz band of the UWL. The start and end times and duration of each observation are listed in Table 3. We only made use of the data above 2.5 GHz in this work, as multi-path propagation through the interstellar medium induces substantial scatter broadening of the pulse profile below this cutoff frequency, resulting in a smearing of the phase-dependent polarization properties [26]. Radiofrequency interference from artificial sources were excised from the data by flagging and zero-weighting the contaminated frequency channels using the paz and pazi tools in psrchive to first remove known persistently affected channels, and then manually flag any remaining interference [44, 45]. The data were then polarization and flux calibrated following the procedure outlined in Ref. [46] using the full receiver model implemented in the pac tool of psrchive. Prior to each magnetar observation, we conducted a short, 80s duration off-source pointing where a linearly polarized switched noise diode of known brightness was injected into the data stream. This was then compared to on/off observations of the calibration source PKS B1934-638 to determine the absolute gain and phase corrections. The polarimetric response of the instrument as a function of parallactic angle was corrected for using a model derived from a rise-to-set track of the bright millisecond pulsar PSR J0437-4725. We then corrected for the effects of Faraday rotation in the Stokes Q and U data due to propagation in the magnetized interstellar medium by applying the known rotation measure of $-1847.6 \,\mathrm{rad}\,\mathrm{m}^{-2}$ using the pam tool with the --aux_rm flag to de-rotate the data to infinite frequency.

3.4 Phase-coherent timing analysis

We obtained ToAs from the radio data by cross-correlating the individual frequency-averaged sub-integrations from each observation with a noise-free template via the Fourier-domain Monte Carlo method implemented in the pac tool in psrchive. The profile template was generated from a set of von Mises functions that were fit to a

fully time/frequency averaged copy of the first Murriyang total intensity profile via the paas tool. We derived X-ray ToAs from the IXPE and NICER data utilizing the Code for Rotational-analysis of Isolated Magnetars and Pulsars (CRIMP). We create an X-ray pulse template from a high S/N NICER profile, which was then fit to a sinusoidal function including only the fundamental harmonic; adding more harmonics did not improve the quality of the fit. We then merge each instrument's event files, and split them into time intervals which incorporate 2000 counts and 4000 counts for NICER and IXPE, respectively, ensuring that each interval is $\lesssim 0.5$ days. Finally, we fit the template to the phase-folded X-ray profiles of each interval, fixing all template parameters except for a phase-shift (i.e., the ToA) and the unpulsed component (which could show mild variability in NICER due to its non-negligible background).

We used the tempo2 pulsar timing package [47, 48] to obtain a locally phase-coherent timing solution covering our radio and X-ray ToAs by re-fitting the magnetar spin frequency and spin-down rate. Both epoch-to-epoch and intra-observation changes in radio-profile shape had minimal impact on the ultimate timing precision. Our resulting timing solution is presented in Table 4.

We then aligned the three Murriyang observations in phase using the timing solution, and then averaged all three together in time and frequency to form a single, average polarization profile. The total linear polarization was computed as the quadrature sum of the Stokes Q and U profiles as $L = \sqrt{Q^2 + U^2}$, which was subsequently de-biased using the method outlined in [49]. The X-ray and radio data are aligned utilizing the DM and TZRMJD parameters presented in Table 4.

3.5 X-ray Spectro-polarimetric Analysis

We performed spectro-polarimetric analysis of the 0.5–12 keV NICER and 2–8 keV IXPE spectral data using Xspec version 12.15.0 to gain insights into the nature of the source emission. For the NICER spectra, we grouped each spectral bin with a minimum of 5 counts per bin and used the W-statistic (c-stat within Xspec) for our statistical fitting. For the IXPE spectra, we grouped each spectral bin according to a minimum of 30 counts per bin and used the chi-squared statistics. Given the source's low S/N at the low-energy bands (< 2 keV), we froze the column density (N_H) to a value of 3.67×10^{22} cm⁻² as reported by Ref. [24]; we additionally used the Wilm solar abundances [50] along with the Verner cross-sections [51] to preserve consistency with the previous analysis. Finally, in the spectral models we impose a calibration constant between each telescope to track the calibration uncertainties during the observation (see Table 1).

We simultaneously fit the NICER SCORPEON background model with the source spectra. During the fits, we froze the normalization of the trapped electron components to 0 since they did not produce any significant contributions to the fitted background. The background models reveal that the NICER source spectra is dominated by the background below $\approx 1.4~\rm keV$ and above $\approx 7~\rm keV$ (see Extended Figure). Likewise, the IXPE spectra are background dominated above $\approx 6~\rm keV$, limiting the statistics of the higher energy contributions.

Historically, the broadband spectrum has been well described using either a 2BB+PL or a BB+2PL fit [23, 24]. However, due to the constrained energies at which

the source is detectable in this data set, these spectra do not significantly capture the hot BB and/or PLs which appear at energies $\gtrsim 6$ keV. We attempted to fit both a single and double BB model and performed an F-test to assess the inclusion of the second BB. We found an F-statistic value of 2.47 and the associated probability as 0.09. While the F-test indicates that including the extra BB component parameter could be reasonable, the 2BB best fit model does not yield physically reasonable values and thus we reject the extra component. Therefore we find that a single absorbed BB is sufficient to accurately describe the spectral shape of this particular data set, with a fit statistic of 1798.80 for 1511 d.o.f. Additionally, we find that applying a linear polarization component to the model performs the best with a total fit statistic of 1798.80 for 1511 d.o.f. compared to 1946.38 for a power-law component and 1840.09 for a constant component for the same d.o.f. Fitting a single absorbed power-law model yields largely unphysical parameters and thus this model was rejected.

We use the Goodman-Weare MCMC method within Xspec with 10 walkers drawn from a multidimensional gaussian with means centered at the best fit model parameters. The MCMC generated three sets of 5000 simulated spectral fits for a total length of 15000. The first 500 from each run were then burned. These runs were used to generate corner plots of the one- and two-dimensional posterior distributions to assess the correlations between the fitted parameters, shown in Extended Figure 5.

3.6 Radio Polarization Analysis

Under the assumption that the radio emission from 1E 1547.0—5408 originates from above the polar cap of an approximately dipole magnetic field component, we can use the rotating vector model of Ref. [33] to constrain the magnetic and viewing geometry of the magnetar. The linear polarization angle can be described as an S-shaped sweep across the profile as

$$\tan(\Psi - \Psi_0) = \frac{\sin\alpha \sin(\phi - \phi_0)}{\sin\zeta \cos\alpha - \cos\zeta \sin\alpha \cos(\phi - \phi_0)},\tag{1}$$

where Ψ_0 is the reference PA at the inflection point of the RVM swing, ϕ is the rotation phase of the magnetar, ϕ_0 is the pulse phase at which the PA inflection point occurs, α is the magnetic inclination angle and $\zeta = \alpha + \beta$ is the viewing angle between the spin-axis and our line of sight, which is in turn the product of the magnetic inclination angle and magnetic impact parameter (β) . We fit the RVM to the average profile obtained from combining our three concurrent *Murriyang* observations, where we sampled the model parameters using the bilby Bayesian inference library [52] as an interface to the dynesty nested sampling algorithm [53]. This was performed using a Gaussian likelihood of the form

$$\mathcal{L}(d|\theta) = \prod_{i}^{n} \frac{1}{\sqrt{2\pi\sigma_{i}^{2}}} \exp\left[-\frac{(d_{i} - \mu(\theta))^{2}}{2\sigma^{2}}\right],\tag{2}$$

where d is the data (corresponding to the PA), $\mu(\theta)$ is the RVM with model parameters given by θ , and σ is the uncertainty on the PA. Note, we modified the formal uncertainties on the PA by adding in an additional error in quadrature term (EQUAD) as $\sigma^2 = \sigma_{\Psi}^2 + \sigma_{\rm EQUAD}$ to account for potential underestimation of the PA uncertainties due to uncorrected systematic effects. We assumed uniform priors on all model parameters, with prior bounds set to $-45^{\circ} < \pi(\phi_0) < 45^{\circ}, -90^{\circ}\pi(\Psi_0) < 90^{\circ}, 0^{\circ} < \pi(\alpha) < 180^{\circ}$ and $-40^{\circ} < \pi(\beta) < 40^{\circ}$. The resulting one- and two-dimensional posterior distributions are displayed in Extended Data Figure 6.

Our recovered values of $\alpha=2.4^{\circ}_{-1.2}^{+1.4}$ and $\beta=2.9^{\circ}_{-1.4}^{+1.7}$ (equating to $\zeta=5.2^{\circ}_{-2.6}^{+3.2}$) indicate 1E 1547.0–5408 is an aligned rotator, viewed almost pole-on. This geometry is seemingly in tension with the previously reported values of $\alpha=160^{\circ}$ and $\beta=14^{\circ}$ from Ref. [26]. However, this can be largely explained by a covariance between the magnetic and viewing angles due to the unknown spin direction of the magnetar. Applying our more modern Bayesian inference based approach to fitting the RVM of the 2007 observation analyzed by Ref. [26], we obtain values of $\alpha=4.9^{\circ}_{-2.4}^{+3.4}$ and $\beta=3.5^{\circ}_{-1.7}^{+2.4}$ (a figure displaying the posterior distributions is available in the supplementary materials), for a viewing angle of $\zeta=8.4^{\circ}_{-4.2}^{+5.8}$. This updated fit is consistent with our 2025 measurements to within the 68% confidence intervals.

An estimate of the radio emission height can be inferred from a combination of the profile width (W) and the measured magnetic/viewing geometry. Assuming a filled emission cone, the beam-opening angle (ρ) can be computed as [54]

$$\cos \rho = \cos \alpha \sin \zeta + \sin \alpha \sin \zeta \cos(W/2). \tag{3}$$

The opening angle is related to the emission height $(h_{\rm em})$ via [55]

$$\rho = 3\sqrt{\frac{\pi h_{\rm em}}{2Pc}},\tag{4}$$

where P is the magnetar rotation period and c is the vacuum speed of light. Typically the value of W is taken to be either the profile width at the 10% or 50% (i.e W_{10} or W_{50}) levels. However, there is a clear, low-intensity precursor component to the radio profile of 1E 1547.0–5408 that is not encompassed by either W_{10} or W_{50} , which if ignored would result in an underestimated beam opening angle, and by extension lower inferred emission heights of $h_{\rm em}=225^{+710}_{-208}\,\rm km$ and $133^{+421}_{-123}\,\rm km$ respectively. After iterating over different on-pulse window sizes, we settled on the 1.5% profile width of $W=W_{1.5}=142^\circ$, which fully encompasses the entire radio profile (Fig 2 top panel). Substituting in this value, and our previous measurements of the magnetic inclination and viewing angles, we obtain $h_{\rm em}=330^{+521}_{-245}\,\rm km$. This is consistent with the bulk distribution of emission heights observed among the broader population of rotation-powered pulsars [56], but is substantially lower than other magnetars [57, 58].

3.7 X-ray Emission Modeling Using MAGTHOMSCATT

The pulse profiles of soft X-ray intensities from NS provide powerful insights into the sizes and locations of hot spots on their surfaces, along with constraints on their geometric parameters, specifically the magnetic inclination α of a dipolar field axis and the viewing angle ζ , both relative to the rotation axis. For magnetars, the polarization measurements obtained with IXPE enable a new dimension in the analysis, both by providing tighter constraints on these parameters, yet also allowing probes of the exotic QED prediction of vacuum birefringence in strong magnetic fields. VB causes the polarization eigenmodes to decouple and rotate adiabatically with the magnetic field up to a certain distance from the surface (the polarization-limiting radius; [20]). Accordingly, the Stokes parameters observed at infinity are determined by the magnetic direction at that location. Without VB, the polarization properties at infinity depend on a convolution of the magnetic field directions on the stellar surface.

To model the anisotropy and polarization characteristics of X-ray emission observed for 1E 1547.0–5408in order to constrain the hot spot locale and stellar geometric parameters, we employ MAGTHOMSCATT, a Monte Carlo simulation that treats polarized radiative transfer in magnetized NS atmospheres. The simulation tracks the complex electric field vector of each photon during its atmospheric transport and magnetospheric propagation. As a result, the complete polarization information of the photon is captured, specifying the Stokes vector $\mathbf{S} = (Q, U, V)$, with V representing the circular polarization. General relativistic light bending and redshifting from the surface to infinity are included: herein we assume the NS mass and radius to be $M_{\rm NS} = 1.7 M_{\odot}$ and $R_{\rm NS} = 12$ km, corresponding to a compactness of $2GM_{\rm NS}/(R_{\rm NS}c^2) = 0.425$ (equivalent to that for $M_{\rm NS} = 1.44 M_{\odot}$ and $R_{\rm NS} = 10$ km). The design, validation, and application of MAGTHOMSCATT are detailed in [32, 34, 35].

The simulation is versatile in treating local atmospheric magnetic field directions, which in turn allows for modeling various hot spot configurations, that is, different shapes and locations. Surface atmospheric emissivities are uniformly distributed across a hot spot, and the intensity and polarization signals observed in a particular direction at infinity are obtained by integrating the intensity and Stokes parameters over all locales within a hot spot. We note that for photon energies well below the cyclotron energy, the local anisotropy and polarization properties at the surface are almost independent of the photon energy [32], and therefore are expected to be insensitive to temperature stratification inside the atmosphere. The influences of QED VB on photon polarization during propagation through the magnetosphere can be switched on or off, as desired. Other elements, such as mode conversion at the vacuum resonance deeper in the atmosphere and field line twists in the magnetosphere, are not yet incorporated.

We performed a suite of simulations with a broad range of geometric parameters, to help examine the surface heat topology and viewing geometry of the system. In particular, we studied different hot spot configurations, which can be classified as either (1) a pole-centered circular hot spot, or (2) an offset hot spot. For the latter, we consider both circular and non-circular shapes. The inclination angle α ranged from 0° (aligned rotator) to 90° (orthogonal rotator) in increments of 2°. The viewing angle ζ ranged from 0° to 180°, divided into 180 bins, while the rotational phase ϕ was

divided into 30 bins per cycle. The Stokes parameters in the simulation are computed using coordinates connected to the spin axis and the line of sight, while the reference direction for the observed Q and U aligns with the celestial North. To account for this difference in coordinate directions, we introduce a parameter $\Delta\phi_{\rm ref}$, ranging from 0° to 180° in steps of 1°. In addition, the zero of phase, $\phi=0$, in the observed pulse profiles (Figure 2) is arbitrary. Therefore, the intensity, Q/I, and U/I pulse profiles in the simulations are displaced in phase such that the position of the simulated X-ray intensity pulse peak coincides with that of the observed one.

The size of each hot spot matches the inferred BB emission region from the best spectral fit model (i.e., $A_{\rm BB}=13~{\rm km^2}\approx 4\pi R^2$, with R^2 being the Stefan-Boltzmann law determination listed in Table 1 for a source distance of 4.5 kpc). For circular hot spots, this corresponds to a half-opening angle of $\theta_{\rm cap}\approx 10^\circ$. For non-circular hot spots, we assume a wedge-shaped configuration for simplicity. The magnetic colatitudes of each wedge extends from the pole ($\theta_{\rm c}=0^\circ$) out to a prescribed value, chosen to be between 15° and 30°; the longitudinal range is then determined from the emission region area $A_{\rm BB}$.

For emission from a pole-centered circular hot spot, scenarios with both α and ζ being small produce very low pulse fraction and, therefore, are disfavored by the intensity data. Moreover, if magnetospheric VB is inactive, the depolarization due to the cancellation of polarization vectors from different surface locales is significant when viewing over the pole. Therefore, we can expect that the radio inferred solutions, $\alpha = 2.3^{+1.5}_{-1.2}$ and $\zeta = 5.2^{+3.2}_{-2.6}$, cannot reproduce the X-ray data, if the hot spot is a centered polar cap. Indeed, we find the best fit for this hot spot configuration is $(\alpha, \zeta) = (2^{\circ}, 20.5^{\circ})$ with the absence of VB (orange curves) being preferred, as shown in the top row in Figure 9. The intensity pulse fraction is under-produced $(\chi^2_{\nu} = 1.56)$, while the phase variation of the Stokes parameters are not well replicated, either with or without VB. Moreover, the viewing direction is inconsistent with the radio inferred value at the 4σ level. Consequently, this hot spot scenario is unlikely. We note that this is the best fitting model within the full surveyed parameter space of system and hot-spot geometries, when VB is deliberately excluded.

The overall best-fit model to the observed pulse profiles of intensity, Q/I, and U/I in the 2–3 keV energy range ($\chi^2_{\rm tot} \approx 122$ for 89 d.o.f.) specifically includes VB. This fit corresponds to a wedge-shaped hot spot of magnetic colatitudes extending from 0° to 17° and longitudes from 0° to 120° as shown in Figure 3. This model strongly favors the presence of VB, and results in $\alpha=0^\circ$ and $\zeta=1.5^\circ$ (intensity $\chi^2_{\nu}=1.09$, Stokes Q/I $\chi^2_{\nu}=3.49$, and U/I $\chi^2_{\nu}=1.97$). The corresponding polarization-limiting radius, where the two polarization modes recouple, is approximately 35 stellar radii. This geometry is broadly consistent with the configuration implied by the RVM best fit parameters for the radio emission. Moreover, the 60° magnetic longitude of its centroid is sufficiently offset from the meridian (longitude zero) that anchors the radio cone to accommodate the phase delay of the X-ray peak relative to the radio one. The case where VB is excluded exhibits strong oscillation due to the mixing of different magnetic field directions on the stellar surface as the star rotates, hence strongly disagreeing with the polarization data ($\chi^2_{\nu}=16.5$ for Q/I, and $\chi^2_{\nu}=9.56$ for U/I; see the orange curves in Figure 3 and Figure 9).

A circular offset hot spot (with VB switched on) with its center located at colatitude $\theta_{\rm c}=10^{\circ}$ and radius $\theta_{\rm cap}=10^{\circ}$ (Figure 9, middle row) provides equally satisfactory results to the Stokes Q/I ($\chi^2_{\nu}=3.20$) and U/I ($\chi^2_{\nu}=1.75$) when compared to the wedge case. However, the intensity fit is of slightly lower quality ($\chi^2_{\nu}=1.45$), leading to a higher combined total χ^2 value of $\chi^2_{\rm tot}\approx144$ for 89 d.o.f.

Finally, when considering the α and ζ as derived from the radio analysis, we find that a circular offset hot spot with its center located at colatitude $\theta_{\rm c}=17.5^{\circ}$ and longitude $\phi_{\rm c}=180^{\circ}$ provides satisfactory intensity fit ($\chi^2_{\nu}=1.23$), yet the polarization degree is overestimated, with the magnitudes of both Q/I ($\chi^2_{\nu}=8.95$) and U/I ($\chi^2_{\nu}=11.62$) being too high at particular pulse phases, and underestimated at others (Figure 9, bottom row).

As an independent test for the presence of VB, we performed an analysis on the observed X-ray PA data using an RVM. In the presence of magnetospheric VB, one can show that the PA phase dependence of completely linearly polarized emergent radiation coincides with the azimuthal angle of the magnetic field direction at the polarization-limiting radius in the reference coordinates, see, e.g., [59]. Consequently, the X-ray PA only depends on the magnetospheric field geometry and should be consistent with the RVM given by Eq. (1), assuming a dipole configuration, and by extension with the geometrical elements derived from the radio RVM fits. To verify this, we fit the observed X-ray PA in the 2–3 keV range with the RVM (Figure 7, bottom left). We note that the geometric parameter distributions derived from the RVM for X rays overlap with those obtained from the radio analysis, although with larger uncertainties due to the lower S/N. The most favorable geometry also corresponds to small α and ζ solutions.

In Figure 10, we show in green a representative case among the good RVM fits, with $\alpha=1.5^{\circ}$ and $\zeta=5.5^{\circ}$, consistent with the radio solution. This conclusion is visually apparent when comparing the X-ray and radio PA swings as displayed in the bottom panel of Figure 2; they both oscillate between similar angles and with a similar slope. In Figure 10, we also show the PA traces obtained from the wedge-shaped hot spot simulations for the best-fit geometry $(\alpha, \zeta)=(0, 1.5^{\circ})$ with and without including the VB effects in blue and orange, respectively. The fit quality using RVM and MAGTHOMSCATT with VB is comparable, with a χ^2_{ν} of 2.12 and 2.51, respectively. Without VB, the strong oscillation exhibited in the Stokes parameters (see Figure 3) leads to a strong variation in the PA, as illustrated by the orange histograms in Figure 10, hence being strongly disfavored due to the observed PA. The fact that the RVM can satisfactorily reproduce the observed PA, with the preferred inclination and viewing angles consistent with those inferred from the radio analysis and X-ray modeling, serves as a complementary piece of evidence, further supporting our conclusion that VB is present.

We note that the best-fit scenario shown in Figure 3 corresponds to a coordinate rotation of $\Delta\phi_{\rm ref}=105^\circ$. However, one can observe from the right panel that the simulated U/I trace (blue) slightly crosses zero at rotational phase $\phi \sim 0.75$, causing PA to switch sign. To avoid such discontinuity and obtain a better agreement with the observed PA, one can slightly shift $\Delta\phi_{\rm ref}$ from 105° to 110°. This shift only marginally

degrades the quality of the fit for Q/I ($\chi^2_{\nu}=3.67$) and U/I ($\chi^2_{\nu}=2.53$), while it does not affect the intensity result.

Finally, while the vacuum resonance is not incorporated in our modeling, the analysis is consistent with the sharp decrease in PD observed between 2 and 4 keV, which would imply a full depolarization at an observed energy $E_{\infty} \simeq 6$ keV (corresponding to a local energy $E \simeq (1+z)E_{\infty} \simeq 7.91$ keV for a typical NS gravitational redshift of $1+z\simeq 1.319$). The resonance energy at a given density is $E_V(\rho)\simeq (1.02~{\rm keV}/B_{14})\sqrt{\rho Y_e}$ [60]. Assuming a hydrogen atmosphere $(Y_e=1)$ and that the vacuum–plasma resonance layer lies at $\rho\simeq 100$ –300 g cm $^{-3}$, a typical range for magnetars [60], our results would imply a surface magnetic field strength B in the range $1-3\times 10^{14}~{\rm G}$, broadly consistent with the value inferred from the source timing properties.

4 Extended Tables

Table 2 Timing and Pulsar Parameters

Pulsar parameters	
R. A. (J2000) ^a	15 ^h 50 ^m 54.124
Decl. (J2000) ^a	$-54^{\circ}18'24.11$
$ u(\mathrm{Hz}) $	0.477856(3)
$\dot{\nu} \left(s^{-2} \right)$	$-4.(4) \times 10^{-12}$
Timing epoch (MJD TDB)	58350
Position epoch (MJD TDB)	54795
$DM (pc cm^{-3})$	697(1)
Time span (MJD)	60760-60770
Solar system ephemeris	DE405
TZRMJD	60764.7495
TZRFRQ	3275.71
TZRSITE	pks

Timing and pulsar parameters of the magnetar 1E 1547.0-5408 from our joint Murriyang + NICER observations

Note. Values in parentheses are the 1σ uncertainties on the last digit. ^a Fixed to values from [61].

Table 3 Observations

Telescope	Observation ID	Start Date (UTC)	Stop Date (UTC)	Total Livetime GTI (ks)
IXPE	04003801	2025-03-26T03:01:52	2025-04-05T00:26:53	499.5
NICER	8020300101	2025-03-26T01:09:00	2025-03-26T15:13:00	1.057
NICER	8020300102	2025-03-27T01:51:01	2025-03-27T20:40:58	1.42
NICER	8020300103	2025-03-28T14:56:37	2025-03-28T22:47:32	1.051
NICER	8020300104	2025-03-31T06:33:41	2025-03-31T08:16:16	0.996
Murriyang	uwl_250326_173709	2025-03-26T17:37:09	2025-03-26T18:29:50	3.171
Murriyang	uwl_250330_171906	2025-03-30T17:19:06	2025-03-30T17:59:36	2.436
Murriyang	uwl_250331_131207	2025-03-31T13:12:07	2025-03-31T13:59:53	2.873

List of Parkes/Murriyang, IXPE, and NICER observation IDs, observation start and end times, and total livetimes used in this analysis.

5 Extended Figures

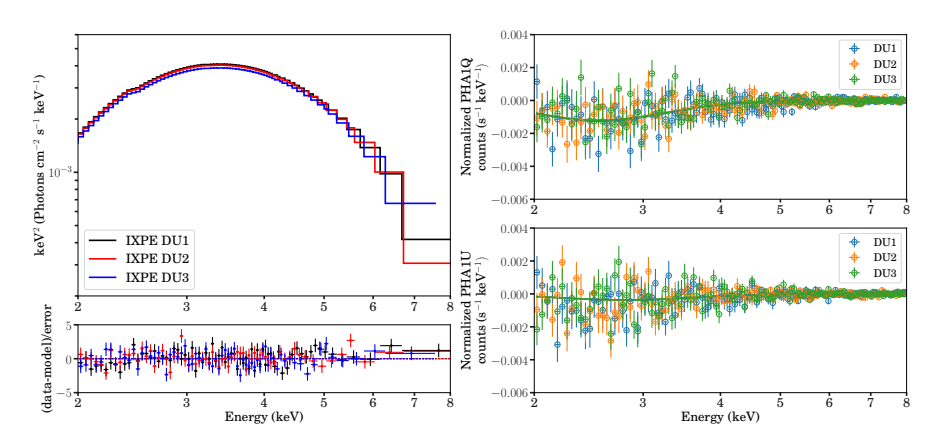
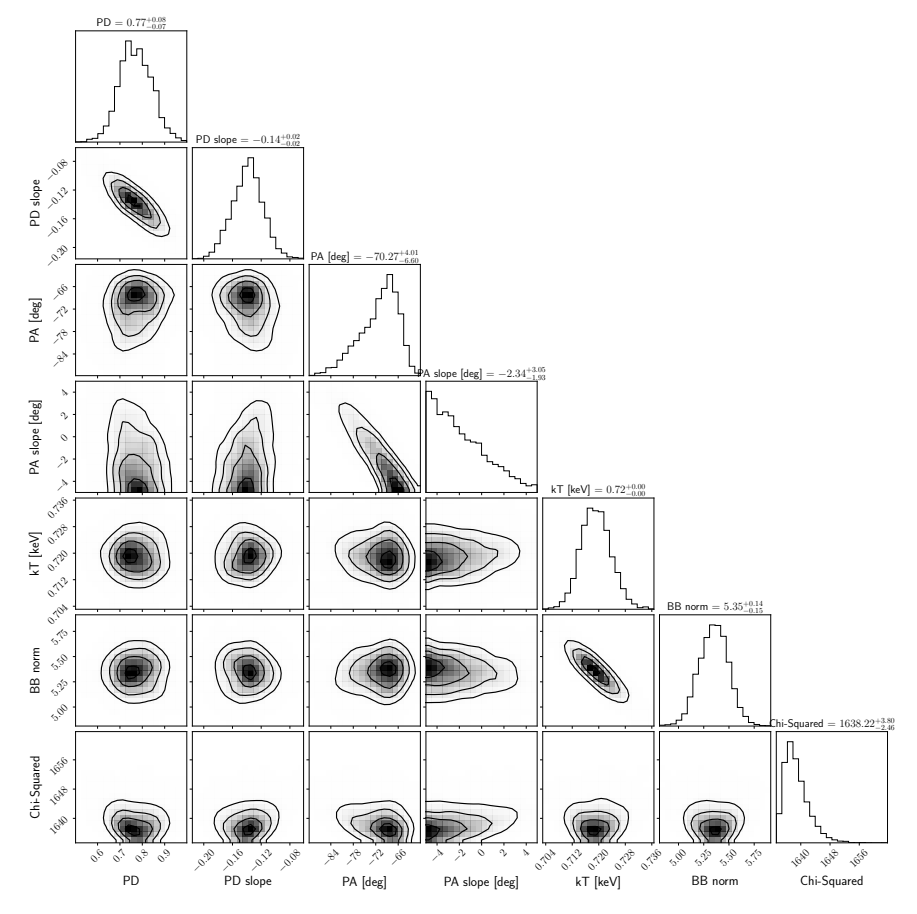
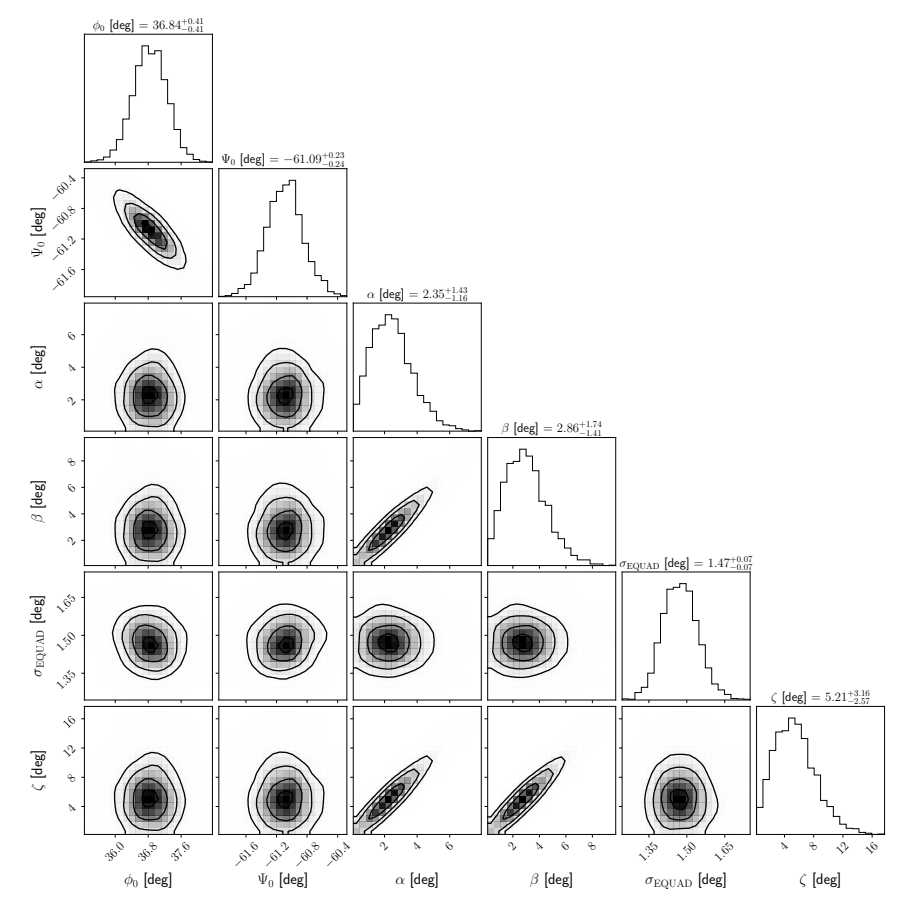


Fig. 4 The simultaneous spectral νF_{ν} models of the NICER+IXPE observations. The upper left panel displays the best fit model, a single absorbed blackbody with a linear polarization component: constant*tbabs(pollin*bbodyrad). NB: Only the IXPE spectra are displayed here for the sake of visual clarity. The bottom left panel shows the data divided by the folded model for the absorbed BB model. The right-hand panels show the normalized Stokes Q/I (top) and U/I (bottom) spectra in linear space for the three IXPE DUs with the solid lines showing the best fit of the linear polarization component. The quasi-thermal BB is accompanied by a strong polarization signal that decreases as a function of energy.



 ${\bf Fig.~5~~Corner~plots~of~the~one-~and~two-dimensional~posterior~distributions~of~the~X-ray~spectro-polarimetric~parameters~produced~by~an~MCMC~chain.}$



 $\textbf{Fig. 6} \ \ \text{Corner plots of the one- and two-dimensional posterior distributions of the radio RVM fit parameters.}$

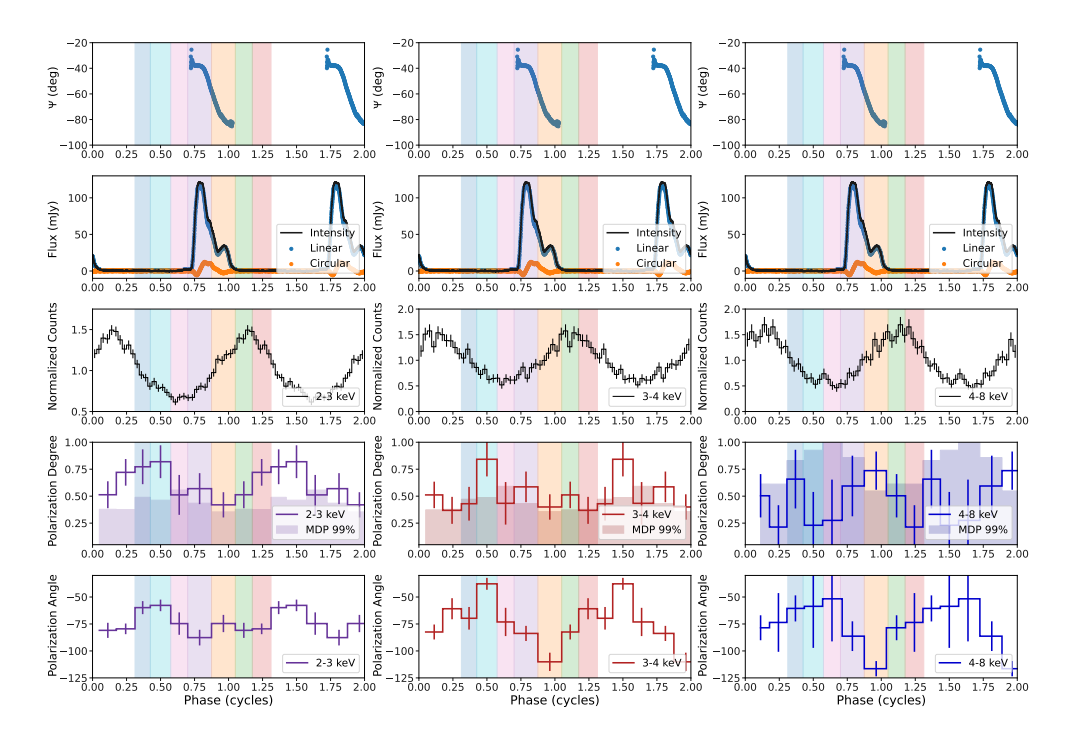


Fig. 7 Complementary plot to Figure 2, with IXPE intensity, PD, and PA (shown in the lower three panels, respectively) binned according to 2–3 keV (left), 3–4 keV (center), and 4–8 keV (right).

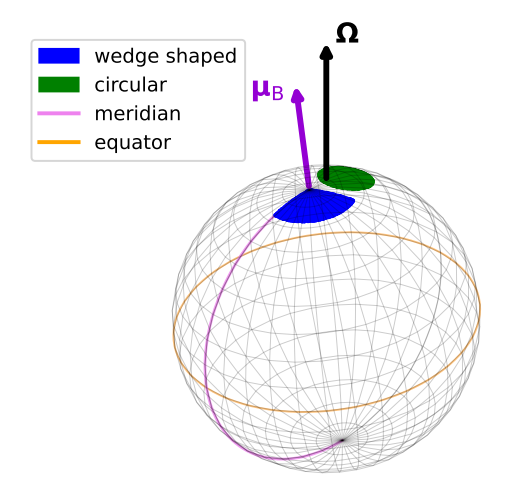


Fig. 8 Illustration of a rotating NS with the magnetic axis $\mu_{\rm B}$ inclined from spin axis Ω . The best-fit wedge-shaped hot spot and an offset circular spot, whose light curves are depicted in Figures 3 and 9 (bottom row), are depicted in blue and green, respectively. The violet (orange) curve indicates the meridian (equator) in magnetic coordinates. The radio cone is centered around $\mu_{\rm B}$.

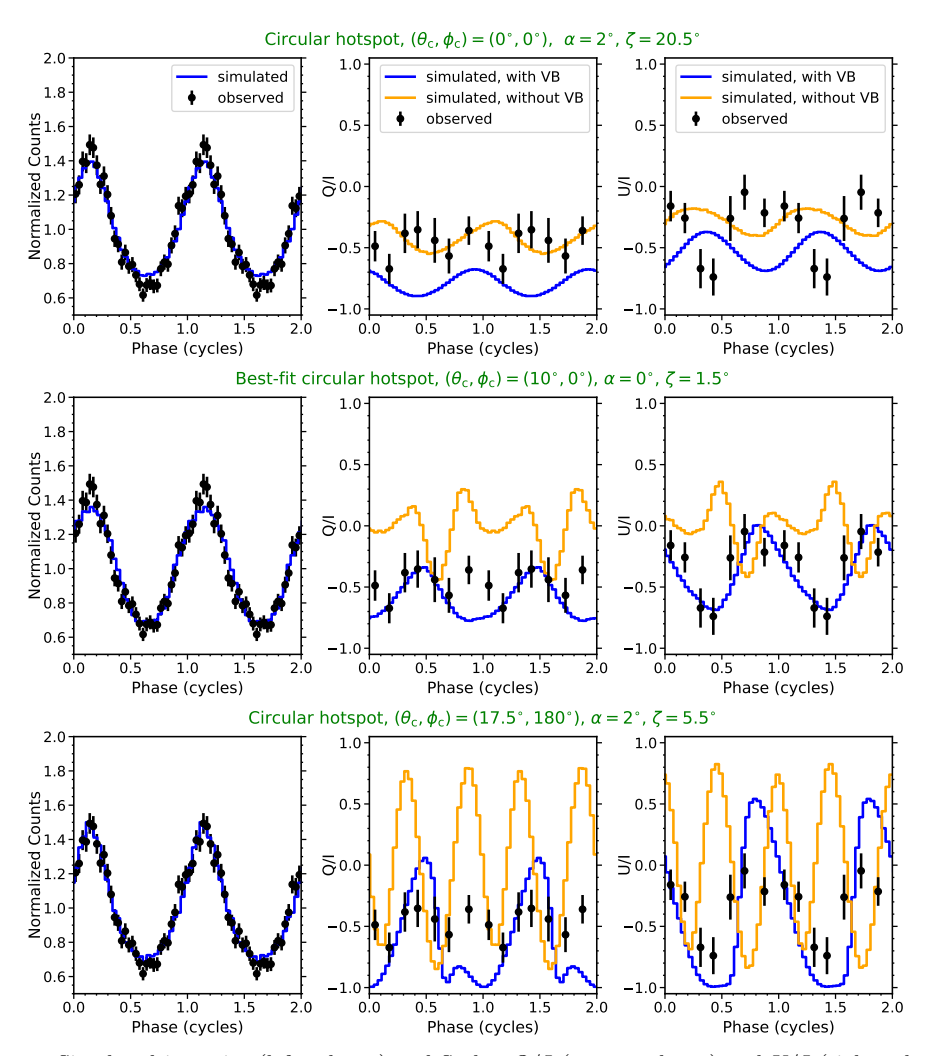


Fig. 9 Simulated intensity (left column) and Stokes Q/I (center column) and U/I (right column) pulse profiles from MAGTHOMSCATT for a single hot spot offset from the magnetic pole as a function of rotational phase (solid lines) for three selected cases: pole-centered circular hot spot (top row), offset circular hot spot with its center located at $(\theta_{\rm c},\phi_{\rm c})=(10^{\circ},0^{\circ})$ (middle row), and offset circular hot spot with its center located at $(\theta_{\rm c},\phi_{\rm c})=(17.5^{\circ},180^{\circ})$ (bottom row). The inclination angle α and viewing angle ζ are indicated. The black dots represent data extracted from IXPE in the 2–3 keV energy range. The blue (orange) solid curves in each panel show the simulated profiles with (without) vacuum birefringence incorporated.

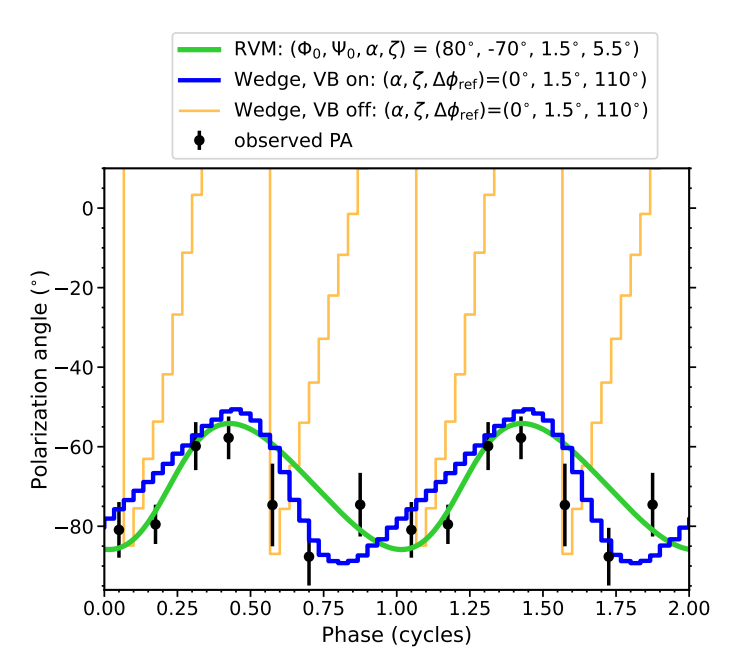


Fig. 10 X-ray polarization angle as a function of rotation phase. The green solid line represents a RVM as given by Eq. (1). The results from the simulation for the wedge-shaped hot spot with (without) VB effects are shown in blue (orange) for the best-fit geometry, $(\alpha, \zeta) = (0, 1.5^{\circ})$. The black dots correspond to the X-ray PA data in the 2–3 keV energy range.

Declarations

Acknowledgments. This work reports observations obtained with the Imaging Xray Polarimetry Explorer (IXPE), a joint US (NASA) and Italian (ASI) mission, led by Marshall Space Flight Center (MSFC). The research uses data products provided by the IXPE Science Operations Center (MSFC), using algorithms developed by the IXPE Collaboration (MSFC, Istituto Nazionale di Astrofisica - INAF, Istituto Nazionale di Fisica Nucleare - INFN, ASI Space Science Data Center - SSDC), and distributed by the High-Energy Astrophysics Science Archive Research Center (HEASARC). Murriyang, CSIRO's Parkes radio telescope, is part of the Australia Telescope National Facility (https://ror.org/05qajvd42) which is funded by the Australian Government for operation as a National Facility managed by CSIRO. We acknowledge the Wiradjuri people as the Traditional Owners of the Observatory site. This project was supported by resources and expertise provided by CSIRO IMT Scientific Computing, and made use of the Ngarrgu Tindebeek supercomputer at the Ozstar national facility at Swinburne University of Technology. The Ozstar program receives funding in part from the Astronomy National Collaborative Research Infrastructure Strategy (NCRIS) allocation provided by the Australian Government, and from the Victorian Higher Education State Investment Fund (VHESIF) provided by the Victorian Government. The material is based upon work supported by NASA under award number 80GSFC24M0006. G.Y. acknowledges NASA support under grants 80NSSC25K7257 and 80NSSC25K0283, through which R.E.S. and A.V.K. are partially supported. M.E.L. is supported by an Australian Research Council (ARC) Discovery Early Career Research Award DE250100508. M.G.B. thanks NASA for generous support under grants 80NSSC24K0589 and 80NSSC25K7257. W.C.G.H. acknowledges support through grant 80NSSC23K0078 from NASA. J.B.C. acknowledges support under NASA award number 80GSFC21M0006.

Data availability. NICER observations are readily accessible on the HEASARC data archive: https://heasarc.gsfc.nasa.gov/W3Browse/nicer/nicermastr.html. IXPE observations will be made publicly available on the HEASARC data archive following the expiration of the proprietary period: https://heasarc.gsfc.nasa.gov/W3Browse/ixpe/ixmaster.html. Radio observations made by Murriyang are publicly available from the CSIRO Data Access Portal (https://data.csiro.au/) following an 18 month proprietary period starting on the observation date.

Code availability. Data reduction and analysis of X-ray products were performed using publicly available software Heasoft version 6.35.0 (https://heasarc.gsfc.nasa.gov/docs/software/lheasoft/) from the High Energy Astrophysics Science Archive Research Center (HEASARC), particularly – FTOOLs v. 6.35.1, SAOImage DS9 v. 8.4b1, and Xspec v. 12.15.0. Generation and calibration of the NICER event lists was also performed by HEASoft's NICERDAS version 12. The simulation and analysis framework ixpeobssim v. 31.1.0 was used to generate high-level IXPE data products: https://ixpeobssim.readthedocs.io/en/latest/. Additionally, the software filterbackground.py was used for treatment of the IXPE background, found here: https://github.com/aledimarco/IXPE-background. Timing analysis was performed using tempo2 (https://github.com/mattpitkin/tempo2), PINT (https://github.com/

nanograv/PINT), and CRIMP (https://github.com/georgeyounes/CRIMP/tree/main). PyXspecCorner (https://github.com/garciafederico/pyXspecCorner) and corner.py (https://corner.readthedocs.io/en/latest/) was used to generate the X-ray spectro-polarimetric and radio RVM corner plots, respectively. Custom code for the MAGTHOMSCATT Monte Carlo simulation and the radio analysis are available upon reasonable request from corresponding authors.

Author's Contributions. R.E.S. performed the X-ray polarization and spectral data analysis and contributed to writing the paper. H.D.T. and M.G.B. led the simulation analysis and theoretical interpretations and contributed to writing the paper. G.Y. is the principal investigator of the IXPE observation presented in this work, which was obtained through the NASA IXPE Guest Observer cycle 2 program. G.Y. performed the X-ray timing analysis and contributed to writing the paper. M.E.L. performed the radio observations and analysis, and contributed to writing the paper. M.N. provided support with the X-ray polarization analysis and contributed to writing the paper. F.C., J.B.C., A.K.H., W.C.G.H., C.P.H, P.K., P.S., A.V.K., and Z.W. provided comments and contributed to the writing of the paper. F.C. is the principal investigator of the Parkes P885 project.